J. Fluid Mech. (2001), *vol.* 445, *pp.* 327–344.
DOI: 10.1017/S0022112001005651 Printed in the United Kingdom

Vibrational effects on convection in a square cavity at zero gravity

By KATSUYA HIRATA[1], TOMOAKI SASAKI[1] AND HIROCHIKA TANIGAWA[2]

[1]Department of Mechanical Engineering, Doshisha University, Kyoto 610-0321, Japan

[2]Department of Mechanical Engineering, Maizuru National College of Technology, Maizuru 625-8511, Japan

(Received 19 May 2000 and in revised form 10 January 2001)

In this numerical study, we investigate natural convection in a two-dimensional square-section enclosure vibrating sinusoidally parallel to the applied temperature gradient in a zero-gravity field. The full Navier–Stokes equations are simplified with the Boussinesq approximation and solved by a finite difference method. Whereas the Prandtl number Pr is fixed to 7.1 (except for some test cases with $Pr = 7.0$, 6.8), the vibrational Rayleigh number Ra based on acceleration amplitude is varied from 1.0×10^4 to 1.0×10^5, and dimensionless angular frequency ω is varied from 1.0×10^0 to 1.0×10^3. In the tested range, time evolutions exhibit synchronous, 1/2-subharmonic and non-periodic responses, and flow patterns are characterized mainly by one- or two-cell structures. Flow-regime diagrams show considerable differences from results in a non-zero-mean-gravity field even at large acceleration amplitudes, and suggest that some parts of non-periodic-response regimes may be related to transitions between flow patterns. The amplitude of fluctuations in spatially averaged kinetic energy density K (equal to the difference between maximum and minimum kinetic energies over a cycle) tends to be large when fluid is stationary everywhere over some interval of time during each period, and has a peak when fluid begins to move continuously throughout one period. Such peaks are caused by impulsively started convection, and are not connected to resonant oscillations in a constant-gravity field.

1. Introduction

This study concerns the system response of buoyantly driven fluid in an enclosure, or a cavity, to oscillatory acceleration at zero-mean gravity, in order to give a better physical insight into natural convection with perturbed acceleration in space. In low-gravity or microgravity environments, we can expect that reduction or elimination of natural convection may enhance the properties and performance of materials such as crystals. However, aboard orbiting spacecrafts all objects experience low-amplitude broad-band perturbed accelerations, or g-jitter, caused by crew activities, orbiter manoeuvres, equipment vibrations, solar drag and other sources. Therefore, there is growing interest in understanding the effects of these perturbations on the system behaviour.

In contrast to many studies concerning g-jitter effects on the system at terrestrial gravity, or on 'Rayleigh–Bénard' convection, there are only a few concerning g-jitter effects at zero-mean gravity. The existence of base, or non-zero-mean, gravity may be unimportant if g-jitter amplitude is much larger than base gravity. However, for smaller amplitudes of g-jitter relative to base gravity, and especially for the onset of

convection, we cannot ignore the existence of base gravity. In fact, the present study will suggest that it remains significant even for rather large amplitudes of g-jitter. Kamotani, Prasad & Ostrach (1981) have analysed two-dimensional square-cavity convection, with zero-mean acceleration, using small-amplitude linearized equations for the fluctuating field and the steady-state equations for the mean field. Their mathematical model is considered to give a good prediction of the system behaviour at low values of the vibrational Rayleigh number Ra. Earlier, Gresho & Sani (1970) conducted a linear stability analysis on a system with non-zero-mean gravity, and showed an analogy to a simple pendulum governed by the Mathieu equation. Their results are not directly applicable to the present study because they relate to small g-jitter relative to base gravity; but it is interesting that g-jitter can destabilize stably stratified fluid and stabilize unstably stratified fluid.

Gershuni & Zhukhovitskiy (1986) summarize several Russian studies, including analytical and fully nonlinear numerical works. These analytical works were based on the method of averaging under the assumption of high-frequency g-jitter. Wadih & Roux (1988) considered a cylindrical container of infinite length in which the applied temperature gradient and direction of g-jitter are parallel to its axis. They proposed some methods to analyse the effect of small-amplitude g-jitter on the stability limits for the onset of convection, by using Floquet theory.

Biringen & Danabasoglu (1990) have solved the fully nonlinear time-dependent Boussinesq equations for g-jitter in a two-dimensional rectangular cavity with an aspect ratio of 2 at $Ra = 1.771 \times 10^5$ and at a Prandtl number $Pr = 0.007$ (germanium). They specified the critical values of ω above which the system experiences transition from convective temperature fields to a conductive one; more specifically, a critical value of about 45 for g-jitter parallel to the applied temperature gradient and about 200–250 when perpendicular to that, where ω is the dimensionless angular frequency of g-jitter (for definition, see the next section). From further calculations for $Pr = 0.71$ (air), they found a Prandtl-number effect inconsistent with Kamotani *et al*'s owing to the omitted nonlinear terms.

Biringen & Peltier (1990) have considered the effects of three-dimensionality as well as full nonlinearity, and computed fluid motion between parallel walls with different constant temperatures and with g-jitter parallel to the applied temperature gradient for $(Ra, Pr, \omega) = (5.7 \times 10^4, 7, 800)$, $(2.28 \times 10^5, 7, 800)$, $(8.82 \times 10^4, 7, 1400)$. Thevenard & Hadid (1991), assuming low Grashof numbers and low Prandtl numbers, have compared a linearized analysis with fully nonlinear simulations for two-dimensional convection between adiabatic walls with g-jitter perpendicular both to the walls and to the imposed temperature gradient.

Kondos & Subramanian (1996) have investigated the effect of frequency by solving the fully nonlinear equations in a two-dimensional square cavity at several values of Ra and Pr. They showed that there is a qualitative difference between low and high frequencies. However, they dealt only with g-jitter perpendicular to the applied temperature gradient, as also did Thevenard & Hadid and the numerical works in Gershuni & Zhukhovitskiy: this problem is simpler than that with g-jitter parallel to the temperature gradient, as will be mentioned later. Grassia & Homsy (1998*a*, *b*) have treated combined thermocapillary- and buoyancy-driven convection in a fluid layer of finite depth but of infinite extent, along which a uniform temperature gradient is imposed. They employed a quasi-steady approach, in the limit of very low forcing frequency. Recently, Suresh, Christov & Homsy (1999) have investigated the same problem, considering small but finite frequency of g-jitter in order to moderate singularities in the quasi-steady model.

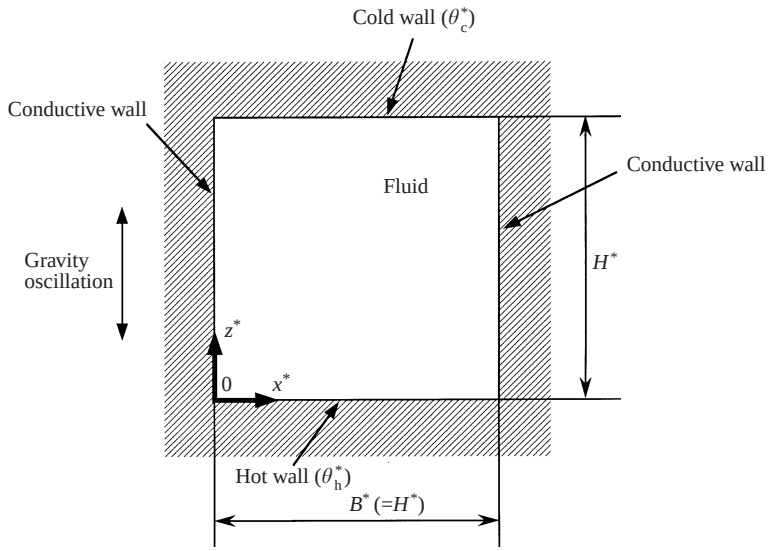

FIGURE 1. Two-dimensional enclosure and coordinate system.

Until now, there have been no experiments or fully nonlinear simulations which systematically elucidate the effects of g-jitter on buoyantly driven flows in a microgravity environment over wide ranges of the governing parameters. And many analytical studies are restricted by the assumption of linearity, quasi-steadiness or very high/low frequency. Therefore, in the present work, we study stability over wide ranges of Ra and ω, solving numerically the fully nonlinear time-dependent Boussinesq equations in a two-dimensional square-section cavity in a zero-gravity field. More specifically, the cavity has perfectly thermal-conducting sidewalls and constant-temperature differentially heated walls at 'top' and 'bottom'. Whereas the Prandtl number is fixed as $Pr = 7.1$ (water) throughout this study except for some test cases ($Pr = 7.0$, 6.8), Ra and ω are varied from 1.0×10^4 to 1.0×10^5 and from 1.0×10^0 to 1.0×10^3, respectively.

For the g-jitter, we assume a sinusoidal acceleration parallel to the direction of the applied temperature gradient. According to Kamotani *et al.* (1981), the g-jitter component perpendicular to the direction of the temperature gradient is the most critical, and the parallel component does not cause appreciable changes in the oscillatory flow field. Their results correspond with the facts that there is no threshold for the onset of the 'Rayleigh–Bénard' convection with horizontally applied temperature gradient and that there is a threshold for fields with vertically applied temperature gradient. But the limited validity of the linear approximation suggests that one must take nonlinearity into account. Accordingly, we may expect that our present system will reveal richer dynamics even at relatively low Ra and ω.

2. Equations and numerical methods

Figure 1 shows the domain to be analysed and the adopted coordinate system (x^*, z^*). All asterisked quantities in this paper are in dimensional form. Fluid in a two-dimensional cavity with a square cross-section is subject to sinusoidal acceleration parallel to the vertical axis in a zero-gravity field. Upper and lower walls, parallel to the horizontal axis, are maintained at constant temperatures θ_c^* (cold) and θ_h^*

(hot), respectively. Sidewalls, perpendicular to the horizontal axis, are assumed to be perfectly thermally conducting. Uneven density of fluid originating from the temperature difference of the walls produces buoyancy and drives convection due to fluctuating acceleration.

The full Navier–Stokes equations in two-dimensional Cartesian coordinates are simplified with the Boussinesq approximation, which leads to the two-dimensional, unsteady equations for continuity, momentum transport and energy transport. In dimensionless form, these can be written as

$$\nabla \cdot \boldsymbol{v} = 0, \tag{2.1}$$

$$\frac{\mathrm{D}\boldsymbol{v}}{\mathrm{D}t} = -\nabla p + Pr\ \nabla^2 \boldsymbol{v} + Ra\ Pr\ \sin(\omega t)\theta\ \boldsymbol{e}_z \tag{2.2}$$

and

$$\frac{\mathrm{D}\theta}{\mathrm{D}t} = \nabla^2 \theta, \tag{2.3}$$

with $\mathrm{D}/\mathrm{D}t = \partial/\partial t + \boldsymbol{v} \cdot \nabla$, $\boldsymbol{e}_z = (0, 1)$, $\nabla = (\partial/\partial x, \partial/\partial z)$ and $\nabla^2 = \partial^2/\partial x^2 + \partial^2/\partial z^2$, where $\boldsymbol{v} = (v_x, v_z)$ is velocity, t is time, p is pressure and θ is temperature. These are non-dimensionalized using the cavity height H^* as the length scale, $\rho^*(\kappa^*)^2/(H^*)^2$ as the pressure scale, the thermal diffusion time $(H^*)^2/\kappa^*$ as the time scale and the thermal diffusion velocity κ^*/H^* as the velocity scale. Here, ρ^* and κ^* are density and thermal diffusivity in dimensional form, respectively. Also we non-dimensionalize temperature as $\theta = (\theta^* - \theta_c^*)/(\theta_h^* - \theta_c^*)$.

If we introduce the vorticity ζ and streamfunction ψ defined respectively as

$$\zeta = \frac{\partial v_z}{\partial x} - \frac{\partial v_x}{\partial z} \tag{2.4}$$

and as

$$v_x = \frac{\partial \psi}{\partial z}, \quad v_z = -\frac{\partial \psi}{\partial x}, \tag{2.5}$$

the continuity equation (2.1) is identically satisfied and need not be dealt with explicitly. Then we can rewrite equations (2.4) and (2.5) as a Poisson equation

$$\zeta = -\nabla^2 \psi \tag{2.6}$$

and equations (2.2) and (2.4) as a vorticity-transport equation

$$\frac{\mathrm{D}\zeta}{\mathrm{D}t} = Pr\ \nabla^2 \zeta + Ra\ Pr\ \sin(\omega t)\frac{\partial \theta}{\partial x}. \tag{2.7}$$

The set of governing equations (2.3), (2.6) and (2.7) contains three parameters, namely, the vibrational Rayleigh number Ra based on the acceleration amplitude η^* of the g-jitter, the Prandtl number Pr of fluid, and the dimensionless angular frequency ω, which are given as follows:

$$Ra = \frac{\eta^* \alpha^* (\theta_h^* - \theta_c^*)(H^*)^3}{\nu^* \kappa^*}, \tag{2.8}$$

$$Pr = \frac{\nu^*}{\kappa^*} \tag{2.9}$$

and

$$\omega = \frac{\omega^* (H^*)^2}{\kappa^*}. \tag{2.10}$$

Here, α^* is the coefficient of thermal expansion, v^* is kinematic viscosity and ω^* is the angular frequency of the forced acceleration. Pr is fixed to 7.1 throughout this paper, except for some test cases. Further, the dimensionless period τ is defined by

$$\tau = \frac{2\pi}{\omega}. \tag{2.11}$$

The governing equations are solved subject to the following boundary conditions:

$$\left.\begin{aligned} &\psi = 0, \frac{\partial \psi}{\partial x} = 0 \quad \text{and} \quad \frac{\partial \theta}{\partial z} = -1 \quad \text{on} \quad x = 0, 1 \quad (0 \leqslant z \leqslant 1), \\ &\psi = 0, \frac{\partial \psi}{\partial z} = 0 \quad \text{and} \quad \theta = 1 \quad \text{on} \quad z = 0 \quad (0 \leqslant x \leqslant 1) \\ &\psi = 0, \frac{\partial \psi}{\partial z} = 0 \quad \text{and} \quad \theta = 0 \quad \text{on} \quad z = 1 \quad (0 \leqslant x \leqslant 1). \end{aligned}\right\} \tag{2.12}$$

The first condition expresses the perfect conductivity of the sidewalls.

The solution procedure of the governing equations is based on the time marching method. All computations were carried out on desktop PCs. The whole computational domain is discretized by an equally spaced regular mesh with a size of 41×41, as well as 21×21 and 81×81 for supplementary confirmation. The time increment was $\pi \times 10^{-6}$ in most cases; but sometimes, especially at high Ra and ω, smaller values were chosen in order to confirm the accuracy of our results. The energy-transport equation (2.3) and the vorticity-transport equation (2.7) are approximated by a semi-implicit approach, that is, the Crank–Nicholson method with second-order accuracy in time. All space derivatives except the convection terms are approximated with central finite differences with second-order accuracy. The convection terms are approximated with a third-order upwind scheme. We solved the finite difference equations by the successive over-relaxation (SOR) iterative method. The convergence of the SOR method is determined when the maximum relative errors reach 10^{-5} for equation (2.3) and 10^{-3} for equation (2.7). At each time step, the Poisson equation (2.6) is approximated by the central finite difference with second-order accuracy, and solved by the SOR method. The convergence of the SOR method is determined when the maximum relative error reaches 10^{-10}. The calculations reported are started with zero-velocity and zero-temperature initial fields, and proceed long enough that these fields become well developed. For sufficient time, we actually needed several τ (here $\tau \equiv 2\pi/\omega$) for $\omega = 10^0$–10^1, several decades of τ for $\omega = 2 \times 10^1$–10^2, and several hundreds of τ for $\omega = 2 \times 10^2$–10^3. This means that the computation time is dominated by thermal diffusion, rather than the imposed period τ.

Upwind discretization of the convection terms introduces a diffusive error, or artificial diffusion, as its leading truncation error term is diffusive. In the present situation, the buoyant force acting on the fluid changes its sign twice during one period due to reversing the forced acceleration; and we find that, in some cases, a virtually zero flow field appears for some finite interval of time during each period. We confirmed that central difference schemes are not free from numerical oscillations at most Ra and ω, even when the mesh is very fine. Of course, the time increments are much smaller than those required for convective and diffusive stability of explicit schemes. The accuracy of simulated results will be discussed in the next section.

Mesh size	$Ra = 2.5 \times 10^4$	$Ra = 4.0 \times 10^4$
21×21	−4.95	−6.59
41×41	−4.98	−6.45
81×81	−4.99	−6.44

TABLE 1. Streamfunction ψ at $(x, z) = (0.25, 0.5)$ in the terrestrial environment (with $\sin(\omega t)$ replaced by 1) for $Pr = 7.0$.

Mesh size	Nu_{mean}	Nu_{amp}
21×21	2.34	0.45
41×41	2.17	0.40
81×81	2.10	0.41

TABLE 2. Time-mean Nusselt number Nu_{mean} and amplitude of Nusselt number Nu_{amp} (difference between maximum and minimum Nu) over the heating parts of walls, in the terrestrial environment (with $\sin(\omega t)$ replaced by 1) for $Ra = 1.0 \times 10^5$ and $Pr = 6.8$.

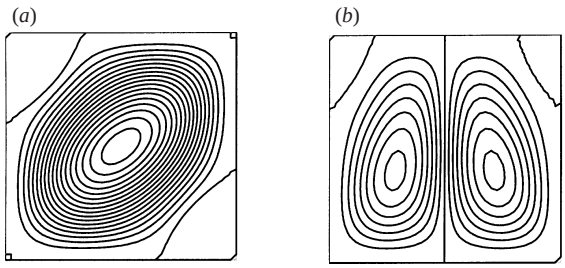

FIGURE 2. Steady convection in the terrestrial environment (with $\sin(\omega t)$ replaced by 1) for $Pr = 7.0$. Streamlines for (*a*) $Ra = 2.5 \times 10^4$, (*b*) 4.0×10^4.

3. Results and discussion

3.1. *Convection in the terrestrial environment*

In order to confirm the accuracy of the numerical method, we conducted a simulation in the terrestrial environment without gravity modulation, namely, using equation (2.7) with $\sin(\omega t)$ replaced by 1. Results for steady motion are shown in figure 2; more specifically, figure 2(*a*) for $Ra = 2.5 \times 10^4$ and $Pr = 7.0$, and figure 2(*b*) for $Ra = 4.0 \times 10^4$ and $Pr = 7.0$. These results coincide with those by Mizushima & Adachi (1997). Table 1 shows the effect of mesh size on numerical accuracy. The flow patterns showed no visible mesh-size effect.

A result for unsteady motion is shown in figure 3; more specifically, for $Ra = 1.0 \times 10^5$ and $Pr = 6.8$. This result is very similar to that of Goldhirsch, Pelz & Orszag (1989), although the Nusselt numbers do not agree exactly. Table 2 shows the effect of mesh size on numerical accuracy. Although we again cannot see any mesh-size effect on the flow patterns, the error is larger than in table 1.

In the present paper, our main concern is the zero-mean-gravity environment with modulation. In order to ensure the robustness of our results, we compared all results (41×41 mesh) with 21×21 mesh results for all data, and confirmed that there is

Mesh size	$Ra = 7.0 \times 10^4$	$Ra = 8.5 \times 10^4$
21×21	16.7	19.6
41×41	17.0	19.3

TABLE 3. Amplitude of streamfunction ψ_{amp} (difference between maximum and minimum ψ) at $(x, z) = (0.25, 0.25)$ for $\omega = 1.0 \times 10^2$.

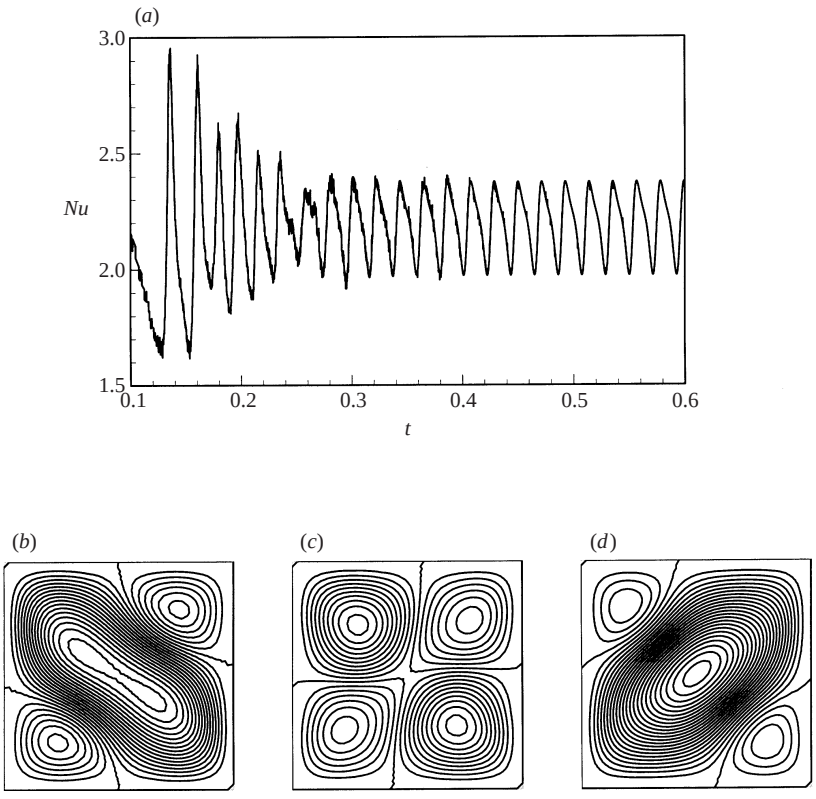

FIGURE 3. Unsteady convection in the terrestrial environment (with $\sin(\omega t)$ replaced by 1) for $Ra = 1.0 \times 10^5$ and $Pr = 6.8$. (*a*) Time evolution of Nusselt number Nu over the heating parts of walls, (*b*) streamlines at $t = 0.5520$, (*c*) at $t = 0.5620$, (*d*) at $t = 0.5700$.

no visible difference between them except for one case. For this one exception, we confirmed that there is no qualitative difference between 41×41 mesh and 81×81 mesh results. Quantitatively, the present problem needs a less fine mesh size than constant-gravity problems. In fact, table 3, which corresponds to the present problem, shows much less error than table 2. This is expected, if we remember that unsteadily forced flow is likely to have much less well-developed boundary layers than steady flow. Even so, at rather high frequency of forcing, computation may yield large error because the changes in the vorticity field are confined to thin regions near walls (Kondos & Subramanian 1996). In the present problem, it will be seen that the flow becomes completely stationary at sufficiently high frequencies, and so we fortunately can avoid this difficulty.

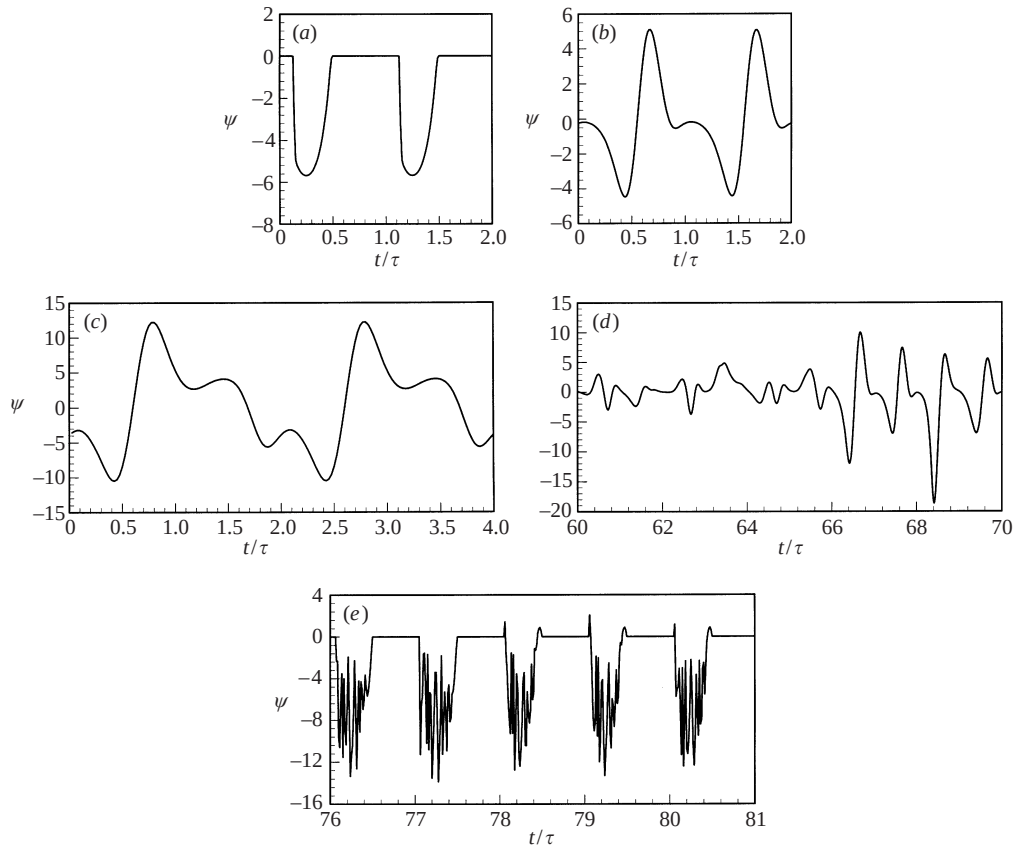

FIGURE 4. Time evolution of streamfunction ψ at $(x, z) = (0.25, 0.25)$. (*a*) $\omega = 1$, $Ra = 3.5 \times 10^4$ (case SY); (*b*) 200, 7.0×10^4 (case SY); (*c*) 500, 1.0×10^5 (case SU); (*d*) 200, 1.0×10^5 (case NP); (*e*) 1, 1.0×10^5 (case NP).

3.2. *Periodicity*

Figure 4 shows time evolutions of streamfunction ψ at $(x, z) = (0.25, 0.25)$ for various values of ω and Ra. Each result is obtained at a time-interval long enough for the system to settle down after the start-up of calculation. Figures 4(*a*) and 4(*b*) are typical examples of a response synchronous with the forced acceleration (hereafter, referred to as case SY), namely, having the same period as the forced acceleration. In figure 4(*a*), during one period, fluid appears to be completely stationary over some interval of time, when the buoyant force is stabilized by the reversed direction of the acceleration. But in figure 4(*b*) flow is maintained at all time, involving higher harmonic waves to some extent. To be exact, while in figure 4(*b*) the flow is synchronous and periodic, that in figure 4(*a*) is synchronous but not exactly periodic, having the alternative of positive or negative amplitudes of ψ each period chosen in a random manner, for the reason mentioned in the next subsection. Figure 4(*c*) is a $1/2$-subharmonic case (case SU), namely, one with twice the forced-acceleration period. Figure 4(*d*) is a case without periodicity (case NP). Figures 5 and 6 show corresponding Poincaré sections at a phase angle of $\pi/2$ relative to the forced acceleration. More specifically, the abscissa denotes the value of ψ at $(x, z) = (0.25, 0.25)$, and the ordinate denotes the value at $(x, z) = (0.5, 0.5)$ at the same moment (figure 5) and the value after one

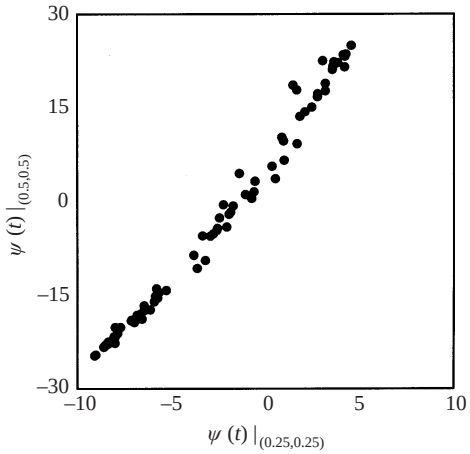

FIGURE 5. Poincaré map for $t = (n + \pi/2)\tau$, with $n = 20, 21, 22, \ldots, 100$. Parameters are as in figure 4(*d*). The abscissa denotes streamfunction ψ at $(x, z) = (0.25, 0.25)$, and the ordinate at $(x, z) = (0.5, 0.5)$.

period at the same place (figure 6). The linearity shown in figure 5 is identical to the flow pattern in space (see also figure 14), while figure 6 highlights its temporally chaotic aspect. Figure 4(*e*) is another example of case NP. This resembles figure 4(*a*), except for fluctuations with higher frequencies. These dominant higher frequencies are close to that for constant-gravity convection with the same Rayleigh number (such as shown in figure 3*a*), and in § 3.3 we will confirm the relation with constant-gravity convection by flow-pattern observation.

The periodicity is broadly summarized in figure 7 as a function of both ω and *Ra*, with so-called regime IV (in Lizée & Alexander 1997) also shown, which will be discussed in § 3.5. We can see that convective motion becomes more stable as ω increases or as *Ra* decreases (regime ST), and that the motion is almost synchronous with the forced acceleration (regime SY) except for three regimes, that is, a 1/2-subharmonic regime around $\omega = 500$ and $Ra > 6.0 \times 10^4$ (regime SU) and two non-periodic regimes around $\omega = 200$ and $Ra > 8.0 \times 10^4$ (regime NP(I)), and for $\omega < 10$ over a wide range of *Ra* (regime NP(II)). Additionally, the shaded area shows where fluid is stationary everywhere over some interval of time during each period τ. In regime SY in this area, we often find random alternation between the solutions with different symmetries, as mentioned above regarding figure 4(*a*).

Mizushima & Adachi (1997) have shown that 'Rayleigh–Bénard' convection becomes unsteady for *Ra* greater than about 5×10^4, and Goldhirsch *et al.* (1989) have found unsteady complex flow fields at $Ra = 1.0 \times 10^5$. Therefore, at *Ra* larger than 5×10^4, we might expect to observe more complicated phenomena. In fact, at $Ra > 5 \times 10^4$, regime NP(II) appears over a wider range of ω. But, even at $Ra > 5 \times 10^4$, the flow is still rather simple, being almost synchronous, at ω larger than 10–20, because the sign of the forced acceleration changes faster than any developing flow field which will might have led to turbulence. In contrast, at $Ra < 5 \times 10^4$, regime NP(II) looks strange, because it seems to be isolated among regimes SY. As will be mentioned later, flow-pattern observation resolves this apparent strangeness.

3.3. *Flow pattern*

Figures 8–13 show sequences of streamlines for various ω and *Ra*; where plots in the sequence are omitted it is because the fluid is stationary at that time. Figure 8

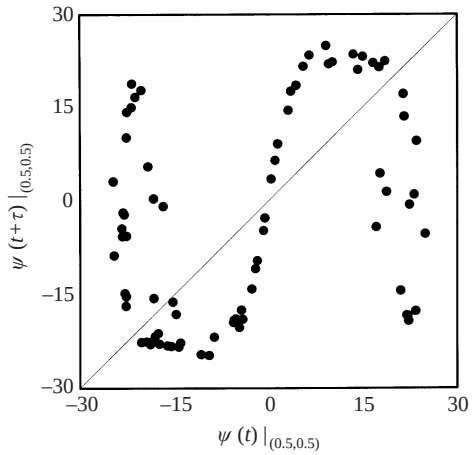

FIGURE 6. Poincaré map for $(x, z) = (0.5, 0.5)$. Parameters are as in figure 4(*d*). The abscissa denotes streamfunction ψ at $t = (n + \pi/2)\tau$, and the ordinate at $t = (n + 1 + \pi/2)\tau$, with $n = 20, 21, 22, \ldots, 100$.

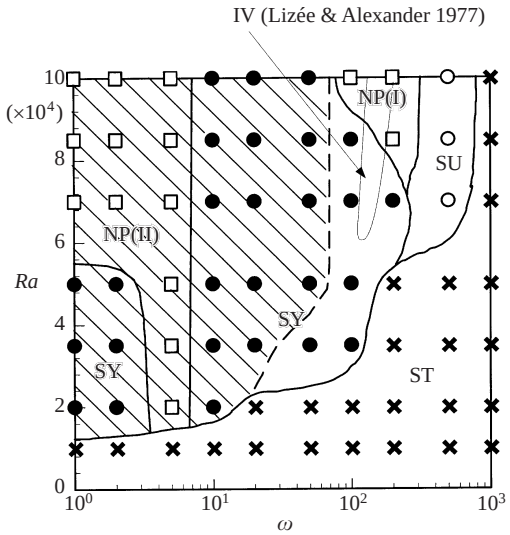

FIGURE 7. Periodicity. ●, synchronous (case SY); ○, 1/2-subharmonic (case SU); □, non-periodic (case NP); ×, stable (case ST). Shaded area shows where fluid is stationary everywhere over some interval of time during each period τ.

shows streamlines for $\omega = 1$ and $Ra = 3.5 \times 10^4$ during one period, figure 9 for $\omega = 10$ and $Ra = 5.0 \times 10^4$ and figure 10 for $\omega = 20$ and $Ra = 7.0 \times 10^4$. Although these figures are all in regime SY (see figure 7), the flow patterns are not similar to one another: in figure 8, the main structure has one cell; in figure 9, it has two cells; and in figure 10(*a–c*), it changes from two to four cells, then breaks symmetry to form one main diagonal cell. Note that the symmetry/antisymmetry of the governing equations and the boundary conditions can lead to other solutions which are obtained by reflecting about the vertical cavity centreline (parallel to the applied temperature gradient), about the horizontal cavity centreline (perpendicular to the gradient), and about both of them. The existence of these reflection solutions (or

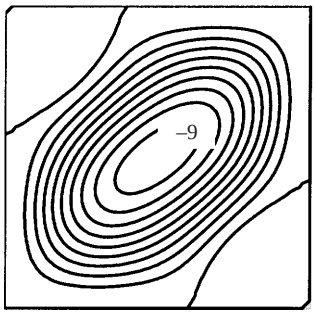

FIGURE 8. A streamline pattern at time $\tau/4$ for $\omega = 1$ and $Ra = 3.5 \times 10^4$. Fluid is stationary at times 0, $2\tau/4$ and $3\tau/4$.

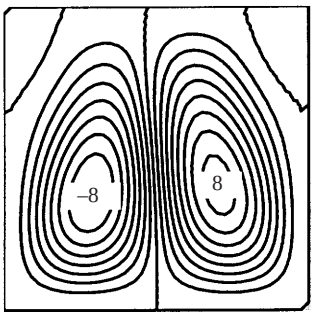

FIGURE 9. A streamline pattern at time $\tau/4$ for $\omega = 10$ and $Ra = 5.0 \times 10^4$. Fluid is stationary at times 0, $2\tau/4$ and $3\tau/4$.

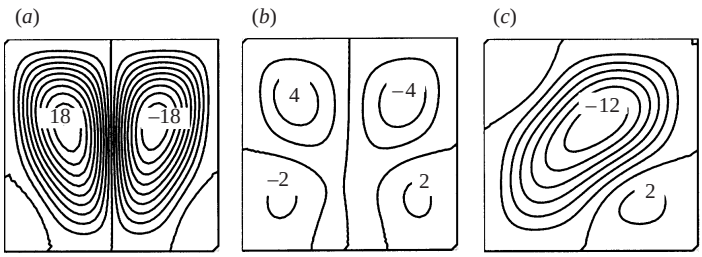

FIGURE 10. A sequence of streamlines for $\omega = 20$ and $Ra = 7.0 \times 10^4$. (*a*) $t = 0.2000\tau$, (*b*) $\tau/4$, (*c*) 0.3750τ. Fluid is stationary everywhere at $t = 0$ and $3\tau/4$.

mirror-image solutions) is a remarkable difference from horizontal-jitter problems. Any one of these four reflection solutions can be simulated, depending on initial conditions. In the case of one-cell or two-cell flow, because two of the four solutions are the same as the other two, we observe only two solutions which are reflections of one another, namely, clockwise/counterclockwise solutions (for one-cell flow) or downward/upward solutions at the cavity centre (for two-cell flow). When fluid is stationary with a conductive temperature field over some interval of time during each period, one or other of the reflection solutions next appears in a random manner. Addition of a tiny asymmetry may result in the appearance of only one member of the reflection solutions, and this is a convenient device for imposition of periodicity. In the present study, however, we did not employ a tiny asymmetry. This random appearance of the reflection solutions is likely to arise in the shaded area in figure 7, which is,

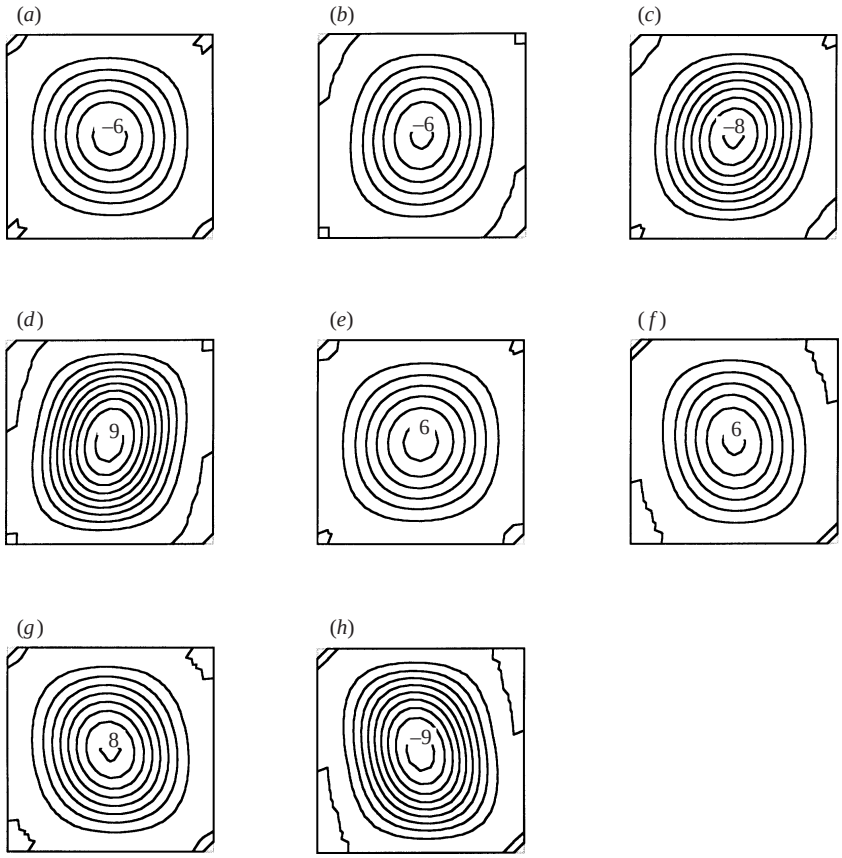

FIGURE 11. A sequence of streamlines for $\omega = 500$ and $Ra = 7.0 \times 10^4$. (*a*) $t = 0$, (*b*) $\tau/4$, (*c*) $2\tau/4$, (*d*) $3\tau/4$, (*e*) $4\tau/4$, (*f*) $5\tau/4$, (*g*) $6\tau/4$, (*h*) $7\tau/4$.

of course, classified as case SY. In fact, we sometimes observed one of the reflection solutions more frequently than the others, because of the passive introduction of a tiny asymmetry by the SOR method.

Other typical samples of observed flow patterns are shown in figures 11, 12 and 13. Figure 11 is for $\omega = 500$ and $Ra = 7.0 \times 10^4$, which is assigned to regime SU in figure 7, and found to be characterized by only one main cellular structure at any time but with rapid sign changes between (*c*) and (*d*) and between (*g*) and (*h*) (see figure 4*c* for reference). Figure 12 is for $\omega = 1$ and $Ra = 1.0 \times 10^5$, which is assigned to regime NP(II) in figure 7. Time t in the figure corresponds to that in figure 4(*e*). As can be seen, one-cell and four-cell flows appear cyclically, which is very similar to convection in a constant-gravity environment (see figure 3). Figure 13 is for $\omega = 5$ and $Ra = 3.5 \times 10^5$, which is also assigned to regime NP(II) in figure 7 but at $Ra < 5 \times 10^5$. This flow pattern seems to fluctuate randomly between one-cell and two-cell flows.

In conclusion, flow patterns observed in the tested range are summarized in figure 14 as a function of both ω and Ra. Here, 1 denotes one-cell flow (see figures 8 and 11); 2 two-cell flow (see figure 9); M starting with two-cell flow and followed by distorted one- and/or four-cell flow (see figure 10); A recurrent appearance of one- and four-cell flows (see figure 12); and F random fluctuation between one- and two-cell flows

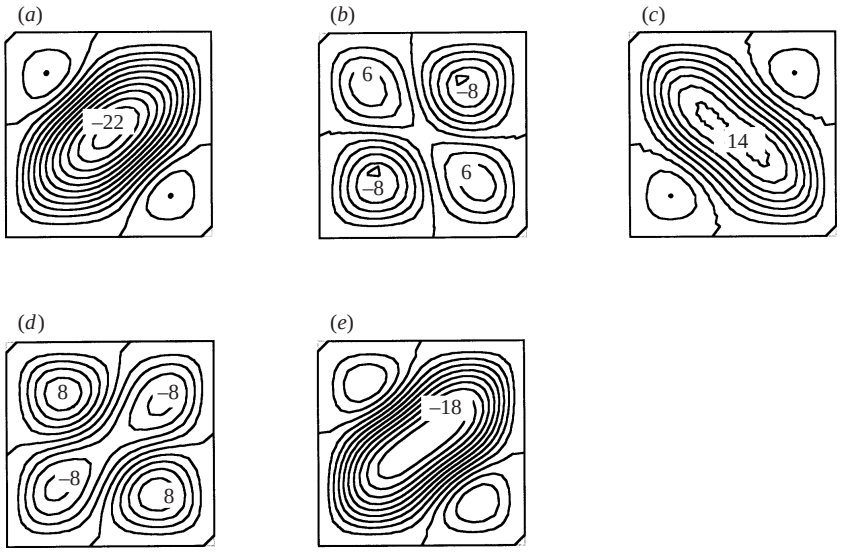

FIGURE 12. A sequence of streamlines for $\omega = 1$ and $Ra = 1.0 \times 10^5$. (*a*) $t = (80 + 0.2000)\tau$, (*b*) $(80 + 0.2125)\tau$, (*c*) $(80 + 0.2375)\tau$, (*d*) $(80 + 1/4)\tau$, (*e*) $(80 + 0.2625)\tau$, (*f*) $(80 + 3/4)\tau$. Values of t correspond to those in figure 4(*e*). The first and last in the sequence, at $t = 80\tau$ and $(80 + 3/4)\tau$, are omitted because fluid is stationary everywhere.

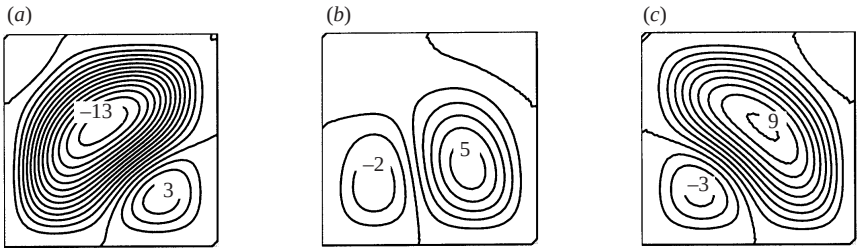

FIGURE 13. A sequence of streamlines for $\omega = 5$ and $Ra = 3.5 \times 10^4$. (*a*) $t = (161 + 0.2250)\tau$, (*b*) $(161 + 1/4)\tau$, (*c*) $(161 + 0.2750)\tau$. The first and last in the sequence, at $t = 161\tau$ and $(161 + 3/4)\tau$, are omitted because fluid is stationary everywhere.

(see figure 13). Most of boundaries in this figure are consistent with boundaries in figure 7, as one might expect. It can be seen that the flow pattern is characterized mainly by one or two cellular structures over the range tested, and that the flow pattern becomes more complicated at Ra larger than about 5×10^5. In regime SU in figure 7, only one-cell flow can be observed. Regime NP(I) and a part of regime NP(II) around $Ra = 2$–5×10^4 nearly coincide with boundaries between one-cell and two-cell flows.

3.4. *Amplitude response*

As a global indicator of responses, we adopt the spatially averaged kinetic energy density K which is defined by

$$K = \frac{1}{2A} \iint (v_x^2 + v_z^2)\, \mathrm{d}x\, \mathrm{d}z, \tag{3.1}$$

where A is the cross-section area of the cavity. Figure 15 shows contours of the amplitude K_{amp} of K, which is the difference between maximum and minimum values

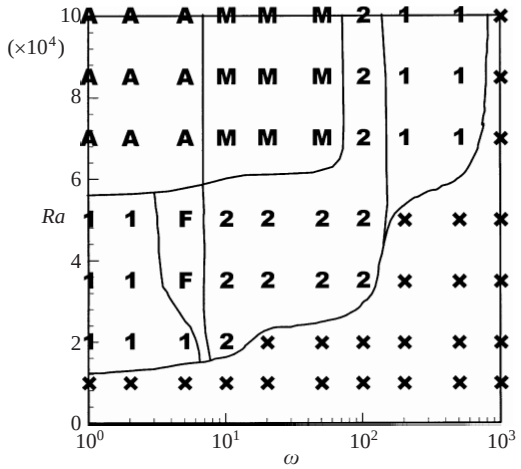

FIGURE 14. Flow pattern. 1, one cell; 2, two cells; M, starting with two cells and followed by one and/or four cells; A, alternation of one and four cells; F, random fluctuation between one and two cells; ×, stable.

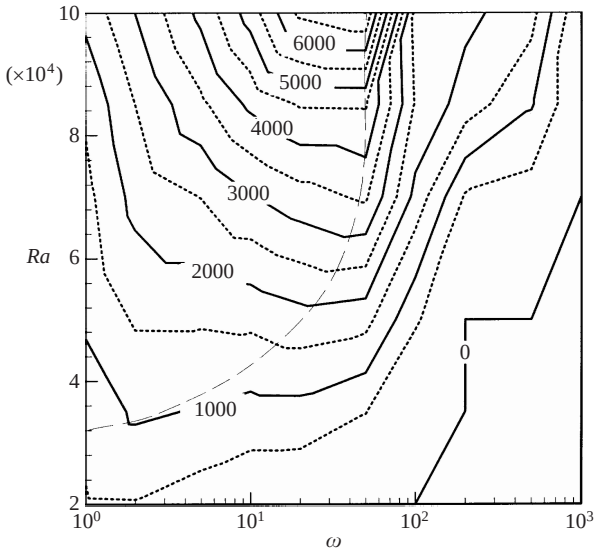

FIGURE 15. Contours of the amplitude K_{amp} of fluctuations in spatially averaged kinetic energy density.

of K during a long period of time. In regime SY of figure 7, when fluid is stationary everywhere over some interval of time during each period, K_{amp} is seen from figure 15 to have larger values, and there is a ridge line (denoted by the broken line in figure 15) close to the boundary of the shaded area in figure 7.

To investigate this ridge line, at $Ra = 5.0 \times 10^4$, phase diagrams are plotted in figure 16 for several values of ω, where the ordinate is the streamfunction ψ at $(x, z) = (0.25, 0.25)$. Flow patterns were always confirmed to be characterized by a two-cell structure whenever ω lies in the range 10–100. Thus, we consider here the results concerning only one member of the two-cell symmetric pair, namely, two-cell flow with the same direction as the applied-temperature-gradient direction at the cavity centre (as shown in figure 9).

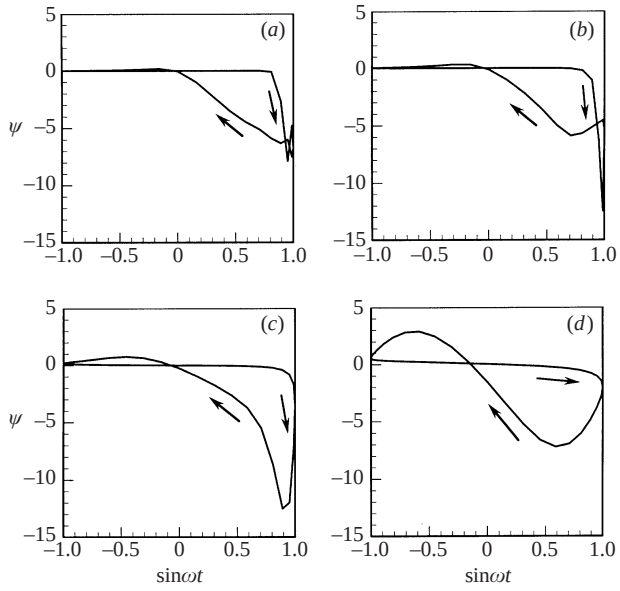

FIGURE 16. Phase diagram at $(x, z) = (0.25, 0.25)$ for $Ra = 5.0 \times 10^4$.
(*a*) $\omega = 10$, (*b*) 20, (*c*) 50, (*d*) 100.

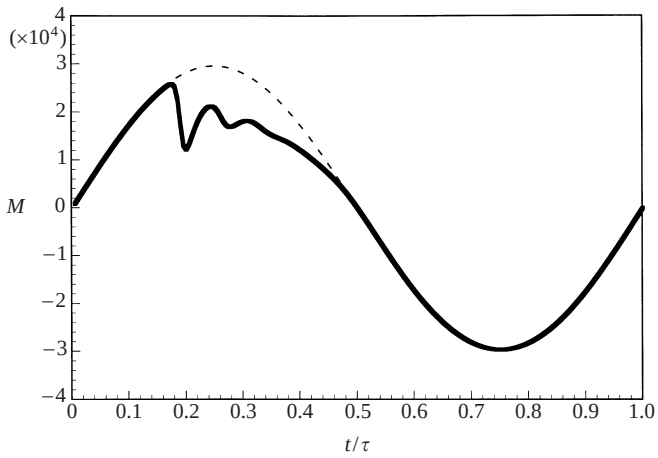

FIGURE 17. Time evolution of buoyancy moment M for $\omega = 10$ and $Ra = 5.0 \times 10^4$.
Broken line is for conductive temperature field.

At $\omega = 10$ (see figure 16*a*), fluid is stationary when $\sin(\omega t)$ is negative because of the stabilizing effect of buoyancy. When $\sin(\omega t)$ changes sign, buoyancy becomes destabilizing, but it is some time before the occurrence of convection, which seems to start suddenly. The (near-) impulsive start of flow yields a minimum of ψ at $\sin(\omega t) = 0.95$. With further increase of t, convection becomes weaker as buoyancy becomes weaker, and finally fluid motion ceases at about $\sin(\omega t) = 0$.

As mentioned earlier, flow patterns are always characterized by two cells, if flow occurs. Here, we introduce the buoyancy moment M defined as

$$M = \frac{Ra\ Pr\ \sin(\omega t)}{A} \iint \theta(\tfrac{1}{2} - z)\,\mathrm{d}x\,\mathrm{d}z. \tag{3.2}$$

Figure 17 shows the time evolution of M corresponding to figure 16(a). The broken line denotes the result for a conductive temperature field with fluid at rest. For t from zero to 0.15, the solid line representing M coincides with the broken line. At $t = 0.2$, an undershoot can be observed, which corresponds to the undershoot in figure 16(a), with a correspondingly increased kinetic energy. After this undershoot and following weak damping, M tends asymptotically to the broken line, when convection has ceased.

On increasing ω, the undershoot in figure 16 becomes deeper and the value of $\sin(\omega t)$ becomes larger at the minimum of ψ. At $\omega = 20$ the undershoot becomes greatest at $\sin(\omega t) = 1$ (see figure 16b). Further increase of ω cannot produce stronger convection than that at $\omega = 20$ because fluid cannot follow a faster acceleration change, which can be seen clearly in figures 16(c) and 16(d). In this way, the ridge line (in figure 15) appears. Further, at $\omega = 100$ (see figure 16d), we can see a remarkable hysteresis effect in which reversed flow persists after $\sin(\omega t)$ becomes negative.

3.5. *Other effects*

Lizée & Alexander (1997) have studied the same problem as here, but with non-zero-mean gravity in the horizontal direction (perpendicular to the applied temperature gradient and to g-jitter). On comparing our results with theirs, it becomes obvious that base gravity (when present) may remain significant even for amplitudes of modulation as large as ten times the base gravity, especially in the case that the base-gravity direction is perpendicular to g-jitter. Their unstable regime IV (see figure 7), in which they observed a Feigenbaum-type route to chaos, roughly seems to agree with our regimes NP(I) and SU. Moreover, flow patterns reported by Lizée & Alexander are all characterized by one cell, as are most of the flow patterns in regimes NP(I) and SU. However, their flow-regime diagram, even at larger Ra or g-jitter larger than the base gravity, looks simpler than our figures 7 (on periodicity) and 14 (on flow pattern), although their tested range of ω is narrower than ours and there is a trivial difference of Pr.

In the asymptotic limit of small ω, the flows at each instant may be compared with those for constant gravity (shown in § 3.1). Namely, as $\omega \to 0$, we can expect to observe during a cycle only one-cell flow around $Ra = 5 \times 10^3$ to 2×10^4, and both one-cell and two-cell flows around $Ra = 2 \times 10^4$ to 5×10^4. Around $Ra = 10^5$, we can expect to observe more complicated flows, including the recurrent appearance of one-cell and four-cell flows over some interval of time.

In the present study, we have considered a situation with perfectly conducting sidewalls. However, insulated-sidewall problems are interesting theoretically and practically: for example, Wadih & Roux (1988) have shown that these two problems display different effects of g-jitter on the onset of convection. Generally, insulated sidewalls impose a different type of symmetric constraint than conducting sidewalls; we expect that two-cell flow will thus appear less frequently than in the present context. In situations such as the transition process from stationary state to turbulence, one cannot ignore this sidewall effect, except at very high Ra. In particular, in the zero-mean-gravity problem, if ω is low, flow may become unstable and then decay at least once a cycle. Moreover, as two-cell flow is frequently observed in the present parameter range, many test cases are regarded to be just at the beginning of the transition process. Therefore, we consider that, within the present parameter range, the sidewall effect on the regime boundaries for two-cell flow may be so large as to cause qualitative changes. On the other hand, we may expect some features to be unchanged such as the existence of regime ST at high ω and low Ra, the

existence of regime A at low ω and around $Ra = 10^5$, and the existence of regime NP around $\omega = 10^2$. As well as more general thermal-boundary conditions, other factors not studied here include other cavity aspect ratios, inclination of g-jitter direction, non-sinusoidal wave form of g-jitter, other Pr values etc.

4. Conclusion

The system response of buoyantly driven fluid in a two-dimensional square cavity to oscillatory acceleration parallel to the applied temperature gradient in a zero-gravity field was studied methodically using a fully nonlinear numerical simulation, at $Pr = 7.1$ (water), $Ra = 1.0 \times 10^4$ to 1.0×10^5 and $\omega = 1.0 \times 10^0$ to 1.0×10^3.

In the range tested, time evolutions exhibit synchronous, 1/2-subharmonic and non-periodic responses, and the flow pattern is characterized mainly by a one- or two-cellular structure. A flow-regime diagram (figure 7) based on periodicity reveals that convection becomes more stable as ω increases or Ra decreases, and that convection is almost synchronous with the forced acceleration except for a 1/2-subharmonic-response regime and two non-periodic-response regimes, some parts of which are isolated among synchronous regimes. A flow-regime diagram (figure 14) based on flow pattern reveals that, for Ra larger than about 5×10^4, convection tends to become more complex: some parts of non-periodic-response regimes appear around boundaries between one- and two-cell-flow regimes, suggesting transition between these flows. Moreover, figures 7 and 14 reveal the influence of base gravity even at relatively large Ra if we compare them with previous results with non-zero-mean gravity.

The amplitude of fluctuations in spatially averaged kinetic energy K tends to be large when fluid is stationary everywhere over some interval of time during each period, and has a peak when fluid begins to move continuously throughout one period. Such a peak is caused by impulsively started convection, and is not connected directly to the resonance with the convection in a constant-gravity field. Thus, the phase shift through such a peak is rather small.

We have shown varied hydrodynamic behaviour in a rather simple system. The behaviour is sometimes much more complicated than one would have expected on the basis of a constant-gravity field, or a modulating gravity field with even a small non-zero-mean component. The present numerical results reveal this complexity even in the averaged quantities that are often important in practical problems. These results may also provide a stimulus for future analytical and numerical work.

We are grateful to the referees and to Professor A. D. D. Craik (St Andrews University) for helpful comments.

REFERENCES

Biringen, S. & Danabasoglu, G. 1990 Computation of convective flow with gravity modulation in rectangular cavities. *J. Thermophys.* **4**, 357–365.

Biringen, S. & Peltier, L. J. 1990 Numerical simulation of 3-D Bénard convection with gravitational modulation. *Phys. Fluids* A **2**, 754–764.

Gershuni, G. Z. & Zhukhovitskiy, Ye, M. 1986 Vibration-induced thermal convection in weightlessness. *Fluid Mech.– Sov. Res.* **15**, 63–84.

Goldhirsch, I., Pelz, R. B. & Orszag, S. A. 1989 Numerical simulation of thermal convection in a two-dimensional finite box. *J. Fluid Mech.* **199**, 1–28.

Grassia, P. & Homsy, G. M. 1998*a* Thermocapillary and buoyant flows with low frequency jitter. I. Jitter confined to the plane. *Phys. Fluids* **10**, 1273–1290.

Grassia, P. & Homsy, G. M. 1998*b* Thermocapillary and buoyant flows with low frequency jitter. II. Spanwise jitter. *Phys. Fluids* **10**, 1291–1314.

Gresho, P. M. & Sani, R. L. 1970 The effect of gravity modulation on the stability of a heated fluid layer. *J. Fluid Mech.* **40**, 783–806.

Kamotani, Y., Prasad, A. & Ostrach, S. 1981 Thermal convection in an enclosure due to vibrations aboard spacecraft. *AIAA J.* **19**, 511–516.

Kondos, P. A. & Subramanian, R. S. 1996 Buoyant flow in a two-dimensional cavity due to a sinusoidal gravitational field. *Microgravity Sci. Technol.* **9**, 143–151.

Lizée, A. & Alexander, J. I. D. 1997 Chaotic thermovibrational flow in a laterally heated cavity. *Phys. Rev.* E **56**, 4152–4156.

Mizushima, J. & Adachi, T. 1997 Sequential transitions of the thermal convection in a square cavity. *J. Phys. Soc. Japan* **66**, 79–90.

Suresh, V. A., Christov, C. I. & Homsy, G. M. 1999 Resonant thermocapillary and buoyant flows with finite frequency gravity modulation. *Phys. Fluids* **11**, 2565–2576.

Thevenard, D. & Hadid, H. B. 1991 Low Prandtl number convection in a rectangular cavity with longitudinal thermal gradient and transverse *g*-jitters. *Intl J. Heat Mass Transfer* **34**, 2167–2173.

Wadih, M. & Roux, B. 1988 Natural convection in a long vertical cylinder under gravity modulation. *J. Fluid Mech.* **193**, 391–415.